



A New Method for the Design of Welding Consumables

An innovative approach using physical and numerical models was investigated to develop welding consumables

BY D. S. TORDONATO, J. C. MADENI, S. BABU, S. LIU, AND P. MENDEZ

ABSTRACT

This work presents a novel approach for the development of welding consumables with the potential of being much faster than standard practice. It is based on the combination of a physical model of the welding process using an arc button melter and the use of thermodynamic and microstructural evolution mathematical models. In the proposed methodology, only small batches of controlled alloys are produced instead of manufacturing an entire spool of wire. The results are then interpreted with existing mathematical models. Another unique aspect of this work is the simulation of welding of microalloyed steels using an arc button melter. This required the controlled addition of small amounts of alloying elements while accounting for their recovery and the control of the oxygen level in the chamber. The microstructure of the button melts was tested for repeatability and compared with published literature. Metallographic examination showed acicular ferrite to be the dominant microconstituent in both the physical model samples and the welded sample; however, the acicular ferrite microstructure in button melted samples was coarser and contained fewer and larger inclusions compared to that of weld metal samples. This research indicates that the button melting technique can effectively represent the microstructural evolution during welding, but improvements are necessary to more accurately reproduce inclusion characteristics.

weld microstructures? A new approach to consumable development utilizing a combination of an arc button melt process and computational thermodynamics was explored in this project to address these questions.

In the arc button melter, a sample is melted in a chamber filled with an atmosphere of controlled composition using a manually controlled gas tungsten arc welding (GTAW) electrode. This method was chosen for its ability to rapidly melt and solidify small samples allowing many candidate alloys to be evaluated in a short time.

Others have also used a similar melting process. Alexandrov and Lippold used an arc button melter in combination with a single thermocouple to characterize phase transformations during cooling, but this work did not involve the creation of new alloys using the technique (Refs. 1, 2). Anderson and Dupont examined solidification modes in stainless steel alloys, in which the effect of oxygen on microstructure is smaller than in microalloyed steels (Ref. 3).

The button melt technique for microalloyed steel is a novel approach to physically simulating the welding phenomena and presents several challenges. First, the technique must accurately reproduce the cooling rates experienced during welding. Second, the alloy composition must be finely controlled to generate repeatable results with microalloys. Finally, oxygen must be introduced into the button in a controlled manner so that inclusions of the proper size, composition, and dispersion are formed. Although introduction of oxygen into the weld metal has been studied extensively for the GMAW and GTAW processes (Refs. 4–22), introduction and control of oxygen during the button melt process is new.

This research evaluated the feasibility of using an arc button melter to reproduce microstructures and inclusion characteristics of the submerged arc welding process.

Introduction

Developments in high-strength low-alloy and microalloyed steels have allowed significant improvements in their properties with just marginal increases in material costs. As base metal strength level increases, the weld metal strength must increase while maintaining adequate toughness; consequently, new welding methods and consumables are also needed. Development of new welding consumables is typically a slow process, which can take many years. The reason is that, traditionally, welding consumables have evolved incrementally as a result of minor adjustments to alloying components. However, as more complex, controlled microstructures are required, it becomes increasingly more difficult to optimize consumable composition simply by

“tweaking” the composition of existing filler metals. The goal of this project was to produce a new methodology suitable for developing welding consumables for a wide variety of applications, especially those requiring microstructures significantly different from the existing ones. This new methodology should avoid the long and expensive process of iterative fabrication of welding wires of different alloys. The above statements lead to the following questions: Is it possible to use a physical model to accurately reproduce the weld microstructure of a specified chemical composition? Is it possible to use existing computational models to gain new insight into the expected nonequilibrium

KEYWORDS

Button Melt
Consumable Design
Consumable Composition
Microstructure
Mathematical Model

D. S. TORDONATO, J. C. MADENI, and S. LIU are with the Colorado School of Mines, Golden, Colo. S. BABU is with The Ohio State University, Columbus, Ohio. P. MENDEZ (pmendez@alberta.ca) is with the University of Alberta, Edmonton, Alberta, Canada.

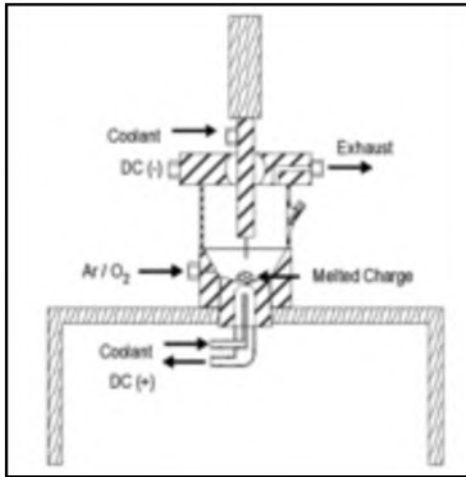


Fig. 1 — Arc button melter apparatus schematic.

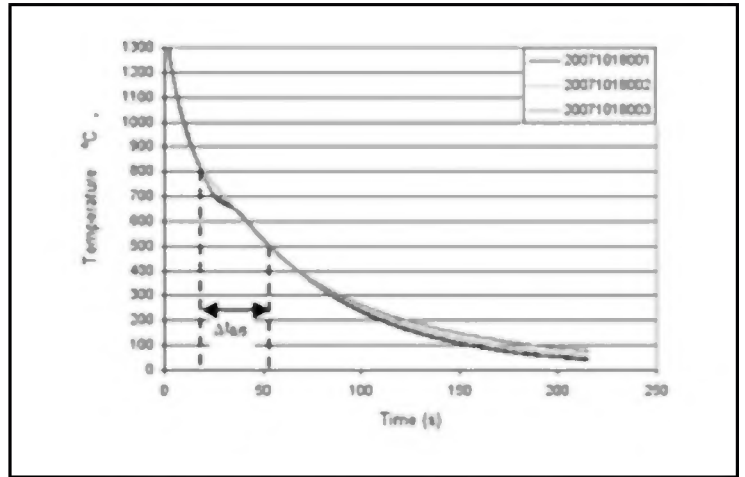


Fig. 2 — Cooling curves for three mild steel buttons. Melting conditions — 150 A, double melted, 20-s melt time, shielding gas flow rate 17.5 ft³/h.

In this research, the ability to control the melt compositions through the addition of various wires, granules, and the addition of oxygen into the shielding gas was investigated. To validate the button melt tests,

Table 1 — Welding Parameters for Sample Ti 13 H (Ref. 23)

Weld Process	SAW
Current	310 A
Voltage	35 V
Travel Speed	4.4 mm/s
Heat Input	2.45 kJ/mm
Plate Thickness	12.7 12.7 mm

The expected cooling rate is $\Delta t_{90} = 30\text{--}35$ s.

weld microstructures studied before in detail by Liu (Refs. 23, 24) were compared with simulated welds in the button melter. Furthermore, the results for each sample were analyzed and compared with predictions made by a numerical model developed by Babu (Ref. 25).

Experimental Procedure

In Liu's study (Ref. 23), several welds were produced with the submerged arc welding process using various combinations of wire, flux, and heat input. Sample Ti 13 H was selected for comparison because of the high fraction of acicular ferrite in the weld metal. The parameters for this weld are listed in Table 1, and the weld bead composition is in Table 2.

Table 2 — Comparison of Measured Composition for SAW Samples and Target Composition for Button Melt Samples

	SAW Sample (Ti 13 H) Measured Composition wt-%	Button Melt Samples Target Composition wt-%
C	0.131	0.131
Mn	0.94	0.94
Si	0.34	0.34
P	0.011	0
S	0.003	0
Cu	0.230	0
O (ppm)	325	325
Cr	0.120	0.120
Ni	0.14	0.370
Mo	0.010	0
Nb	0.140	0.140
Ti	0.0033	0.0033
Al	0.009	0.009
Zr	0	0
B (ppm)	0.0006	0.0006
CE	0.395	0.393

The IIW carbon equivalent is calculated for each composition.

This composition was the target for the final composition of the button with some minor changes: no phosphorus, sulfur, zirconium, or molybdenum was added intentionally. Phosphorus and sulfur are typically regarded as impurities and molybdenum and zirconium were present only in small amounts in the sample composition. Furthermore, for simplicity, additional nickel was substituted for copper. While copper and nickel will have different corrosion protection effects in high-alloy compositions, for the purposes of this experiment, they are considered interchangeable as they are both face-centered cubic alloy additions with similar atomic weights and sizes, and they function as solid-solution strengtheners and austenite stabilizers. They also yield an identical carbon equivalent number of 0.393 according to the IIW formula (Ref. 26).

Controlling the composition so that the button melt chemistry is close to the target chemistry presented a challenge. The additions of some elements, such as boron, are exceedingly small; also, in the presence of oxygen, elements may oxidize and float to the button's surface. Furthermore, some elements may vaporize in the molten pool. It is necessary to account for these changes by accounting for recovery of the ingredients. Recovery is defined as the weight fraction of element in the button after the melting process (present in solution or as a precipitate) divided by the weight fraction of element present in the charge. In this work, the expected recovery for each element was taken from previous experiments conducted with the arc button melter (Ref. 27). These previous button melt experiments indicated that recovery of strong deoxidizing elements, such as titanium and aluminum, is dependent on the amount of oxygen present

in the button. To achieve the target values, the charge of each ingredient was determined as the target value divided by the expected recovery. A total of five samples (labeled A–E) were prepared, each with the same nominal target composition to assess repeatability.

Melting Process

A schematic showing the arc button melt apparatus is shown in Fig. 1. In this system, the melting torch consists of a tungsten electrode held in place by a water-cooled copper sheath attached to a wooden handle. The electrode is mounted in a plastic ball and socket joint, allowing it to rotate, and slide up or down while melting. The sample is placed on a water-cooled copper crucible, which is held in place by a set of clamps. Two types of enclosures were used in the experiments: a sealed glass cylinder, and a glass cylinder with a small port for thermocouple insertion.

Initial experimental work was undertaken to develop a melting process to yield repeatable melting, mixing, and cooling characteristics (Ref. 27). The resulting procedure is detailed in the Appendix. During the melting process, the raw materials formed a completely molten pool, which was approximately 20 mm in diameter and 10 mm in height. The arc size was maintained at roughly the same size as the molten button by adjusting the tip-to-work distance. The button was flipped and a second melting cycle was performed to ensure adequate mixing of the ingredients.

Experimental trials were performed to examine cooling characteristics of this particular process. The Δt % time was measured to be 32–35 s based on data recorded using a bare wire thermocouple harpooned into the button during solidification. Time-temperature profiles for three trial runs are shown in Fig. 2. The cooling rate is a function of the melting process and the experimental apparatus including the water-cooling copper crucible. The measured Δt % time is representative of a submerged arc welding (SAW) process and the welds created by Liu.

The target oxygen content of 350 ppm was obtained by using 145 cm³/min of O₂ and 17.5 ft³/h of argon. This is in accordance with correlations developed in initial trials (Ref. 27). Early attempts to use oxidized iron in various sizes and quantities to control oxygen content were unsuccessful as little oxygen was transferred to the button.

Chemical Analysis

Three types of chemical analyses were performed for the melted buttons to evaluate the as-solidified composition: gas fu-

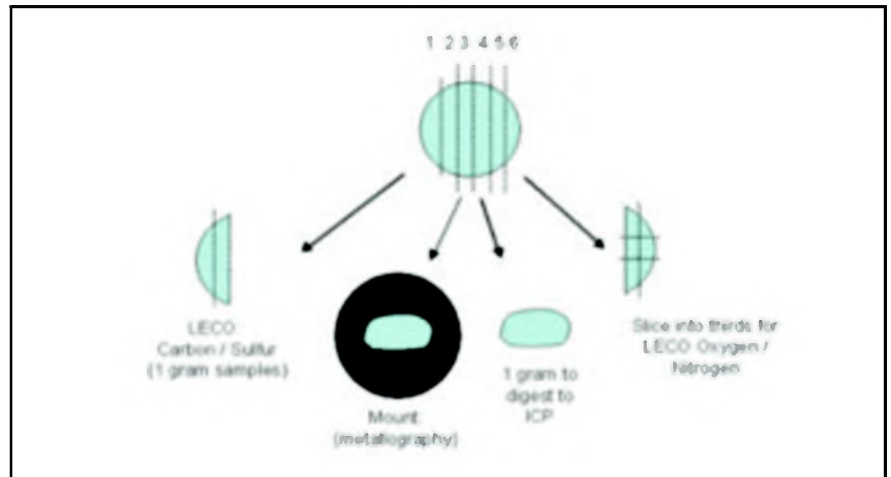


Fig. 3 — Sectioning diagram for analysis of buttons.

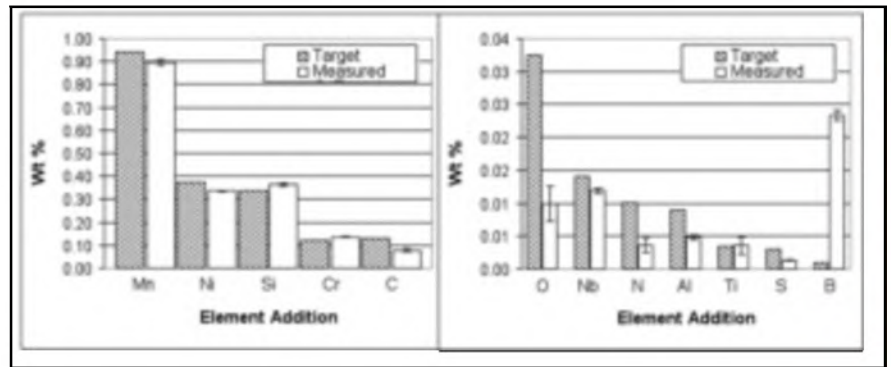


Fig. 4 — Comparison of results from chemical analysis of four identical buttons with the target composition with error bars showing the standard deviation.

sion for oxygen and nitrogen determination (LECO Model TC-436), infrared detection for carbon and sulfur (LECO Model CS-400), and inductively coupled plasma atomic emission spectrophotometry (ICP-AES) for the remaining components. Details concerning the ICP process can be found in Ref. 28.

Arc button melt samples were sectioned for analysis as indicated in Fig. 3, and chemical analysis using inductively coupled plasma was performed on samples A, C, D, and E to determine composition. A portion of sample B's contents was lost during the digestion process and no results were reported. After melting, the buttons were ground to remove the oxide layer on the surface, and then sectioned for analysis and digested using a two-step process. The first digestion step used a dilute nitric acid/deionized water solution. This process dissolved the matrix but left behind a significant amount of second-phase particles, such as oxides. The contents were filtered, and the filtrate was subsequently dissolved in a second

step with a stronger solvent consisting of reagent grade nitric acid, hydrogen peroxide, and sulfuric acid. Because each solution was analyzed separately, the results provide some insight into the chemical composition of oxides or other second-phase particles. One blank sample, i.e., a solution containing no digested metal, was analyzed with ICP to give a baseline for each element. The results of the blank sample were subtracted from the other samples. This was done to correct for any possible error resulting from dissolution of the glassware.

Following the wet chemical analysis, each of the five samples was analyzed for carbon, sulfur, oxygen, and nitrogen using the LECO determinator instruments. Figure 4 summarizes the results of the chemical analysis of all of the buttons. Table 3 shows a comparison of the expected and measured recovery fractions for each element. The error bars in Fig. 4 indicate the variability of each element between the four buttons; each bar is plus or minus a single standard deviation. Variability is

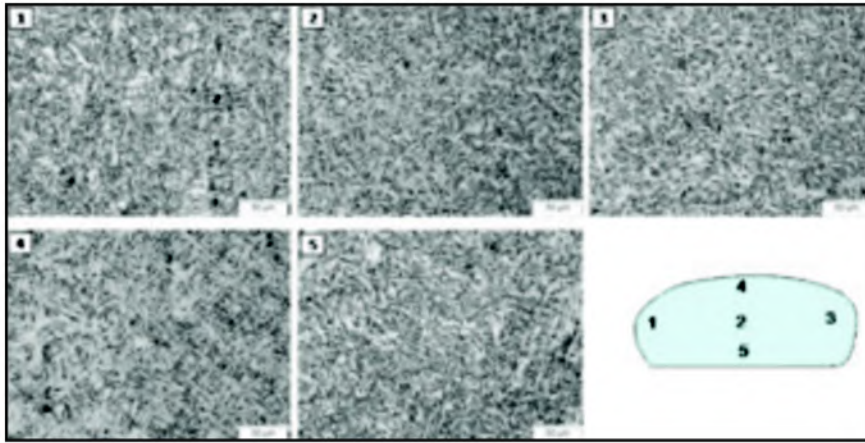


Fig. 5 — Sample micrographs at various positions within sample E.

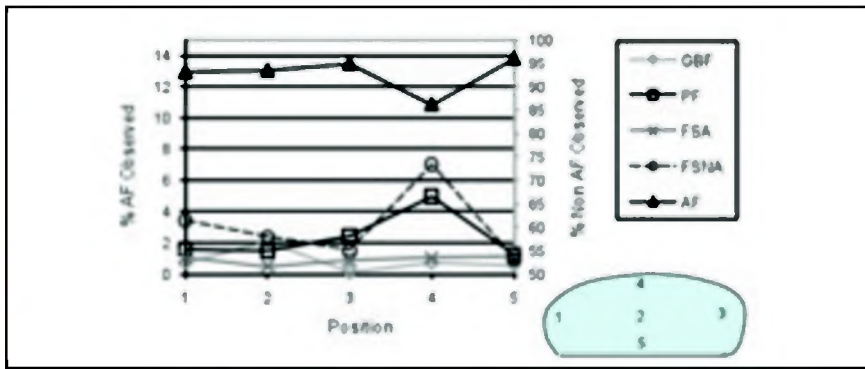


Fig. 6 — Averaged results of quantitative metallography by position. The area fraction observed for each microconstituent is shown as a function of position.

Table 3 — Expected Recovery of Alloying Additions in Button Melt Process (percentage)

	Expected Recovery	Average Recovery (Measured)	Standard Deviation
C	0.93	0.57	0.050
Mn	0.85	0.80	0.008
Ni	1	0.90	0.002
Cr	0.8	0.87	0.007
Ti	0.5	0.61	0.211
Si	0.8	0.86	0.017
Al	0.5	0.25	0.015
Nb	1	0.82	0.124
B	0.9	15.93	3.788

Table 4 — Elemental Composition Averages of Four Button Melt Samples Determined from Each Dissolution Step

Element	Total (wt-%) in Button	Standard Deviation	Amount Present in Precipitate (wt-%)	Standard Deviation	Amount Present in Precipitate (μ grams)
Mn	0.8971	0.0133	0.0006	0.0002	60
Ni	0.3357	0.0011	0.0001	0.0000	10
Si	0.3647	0.0069	0.0011	0.0016	106
Al	0.0049	0.0004	0.0037	0.0011	375
Ti	0.0036	0.0013	0.0011	0.0003	105
B	0.0233	0.0008	0.0003	0.0004	26
Cr	0.1361	0.0018	0.0001	0.0000	7
Nb	0.0119	0.0004	0.0005	0.0001	48

negligible in most of the alloying additions with the exception of titanium, nitrogen, and oxygen. No attempt was made to control nitrogen in the system. In most cases, the measured compositions were within 10% of the target range. Oxygen and aluminum, however, were significantly lower than expected. The aluminum was likely lost due to deoxidation and formation of a surface slag. No attempt was made to characterize the surface slag of these particular samples. Boron exhibited very low variability, an indication of good experimental control; however, the mean measured value was approximately ten times greater than the target value. In previous trials (Ref. 27), the level of boron was within 30% of the target value. The large amount of boron is most likely due to a measurement error during the alloying process. The recovery of nickel was 10% lower than expected at 90% with very little variability between samples. This may be due to analytical error in the ICP instrument.

Table 4 shows a breakdown of the fraction of each element dissolved in the dissolution step. A large fraction of the aluminum and titanium were insoluble in the dilute nitric acid suggesting that they formed oxide inclusions. A small fraction of the manganese, silicon, boron, and niobium was also insoluble. Thermodynamic models suggest the formation of a carbonitride phase containing chromium and niobium for similar low-alloy steel compositions undergoing Scheil solidification (Ref. 27). Assuming that all chromium and niobium formed carbonitrides and the remaining elements formed oxides, the data from Table 4 can be used to estimate bulk oxide composition to be Al 55%, Si, 15.6%, Ti 15.5%, Mn 8.8%, B 3.7%, and Ni 1.4% (wt-%).

Microstructural Analysis

Following chemical analysis, a vertical cross section from each button was mounted in Bakelite for metallographic examination. The samples were ground, polished to 1 μ m, and etched with a 2% nital solution. Each button was examined at 200 and 500 \times magnification with an op-

tical microscope. Sample micrographs for several locations within the button cross section are shown in Fig. 5. In general, the microstructure was predominantly acicular ferrite. A point counting technique was used to quantify the relative volume fractions of each microconstituent present according to the IIW classifications (Ref. 29). The microconstituents considered included acicular ferrite (AF), grain boundary ferrite (GBF), primary ferrite (PF), ferrite with aligned and nonaligned second phase (FSA, FSNA), pearlite (P), and martensite (M). Point counting was performed for samples A, C, D, and E. The micrographs taken at 200 \times were enlarged to 8½ \times 11 in. (22 \times 28 cm) and used for point counting by superimposing a transparent grid of 36 \times 27 yielding approximately 1000 points. Figure 6 shows the volume fraction variation with position. The values represent the average for all four samples analyzed at each position.

In all microstructures, very little to zero GBF and PF was observed. This is likely due to the presence of boron, which segregates to the grain boundaries and suppresses the formation of grain boundary ferrite (Ref. 30). Locations near the top of the button contained slightly less acicular ferrite than bottom locations. The difference can be attributed to the more rapid cooling rates experienced at the bottom of the button.

The microstructures were compared to those observed in Ref. 23, in particular sample Ti 13 H, which is shown in Fig. 7. In sample Ti 13 H, the microstructure consists primarily of fine acicular ferrite (68% AF) with 18% GBF, and 15% FSA/FSNA. One obvious difference between the welded microstructure of Ti 13 H and the button melt microstructure is the lack of grain boundary ferrite present in the button melted samples. Also, the ferrite laths are finer in the Ti 13 H microstructure. The dispersion of oxide inclusions plays an important role in determining the acicular ferrite morphology, and might be affected by the time and temperature history during the melting and resolidification of the sample. As noted in the Appendix, the button melts using the technique described in this work spend a longer time in the molten state (20–25 s per melt) than the weld they intend to represent. This is due to the hold time required for homogeneous mixing to occur. The effect of this longer molten time will be discussed later.

Solidification should begin at the crucible interface and propagate upward in a direction perpendicular to the maximum temperature gradient. The solidification pattern is not expected to drastically alter the size distribution of the inclusion but there would be an effect on the spatial distribution assuming that inclusion trapping occurs in interdendritic spaces. No at-

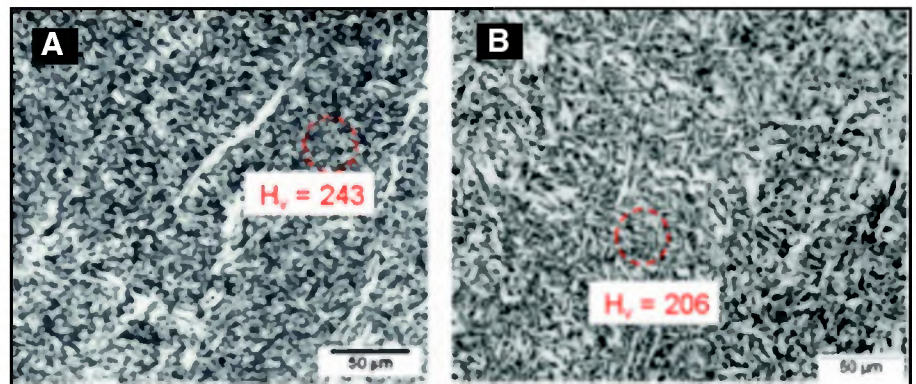


Fig. 7 — Comparison of A with B. A — SAW Ti 13 H sample (Ref. 23); B — button melt (model) sample. Both microstructures contain a large fraction of acicular ferrite, but the welded sample has a finer microstructure.

tempt was made to characterize the spatial distribution of the inclusions. Examination revealed no lateral variation in the microstructure.

Microhardness

Vickers hardness measurements were recorded for the microconstituents in the button melt samples. The typical load and dwell time was 200 g for ten seconds. In several cases, it was necessary to reduce the load to 50 g to affect only the region of interest. Typical values for acicular ferrite ranged from approximately 190 to 220 H_V . Values for GBF, FSA, and FSNA also fell

within this range. The lowest hardness measurement was 177 H_V for PF. Acicular ferrite laths create a finer microstructure when compared to primary ferrite or grain boundary ferrite; therefore, the flow stress and hardness are expected to be higher due to the Hall-Petch effect; however, no attempt was made to quantify the acicular ferrite lath size. This observation is in agreement with Vickers hardness data of our arc button melts, and sample Ti 13 H with AF, FSA, and FSNA microconstituents having similar hardness values and grain boundary ferrite having a much lower value. Hardness of each microconstituent in the button melt samples, how-

Table 5 — Comparison of Predicted Inclusion Composition (wt-%) Using the Babu Model

	Ti 13 H Cooling Rate	Sample A Cooling Rate
Al	50.1	51.5
Ti	19.5	14.2
Si	23.8	23.6
Mn	6.6	10.6
S	0.0	0.0

Button melt composition of sample A under button melt conditions (25-s solidification time) and button melt composition under expected solidification conditions for SAW of sample Ti 13 H.

Table 6 — EDS Analysis for Extracted Inclusions. Compositions in at.-%.

	Ti 13 H (Average for 51 inclusions)	Sample A (Average for 20 inclusions)
Mn	31.9	33.4
Si	29.7	23.8
S	4.4	0.0
P	0.5	0.0
Al	12.2	30.0
Ti	2.6	9.8
Fe	17.7	0.0
Mo	0.0	3.0

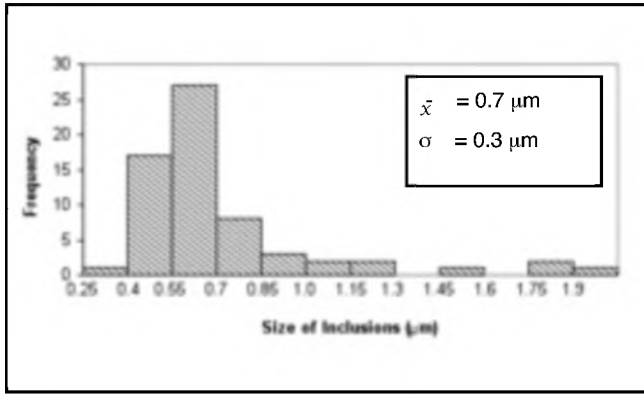


Fig. 8 — Histogram of inclusion sizes observed in the carbon extraction replica of sample A (button melted sample).

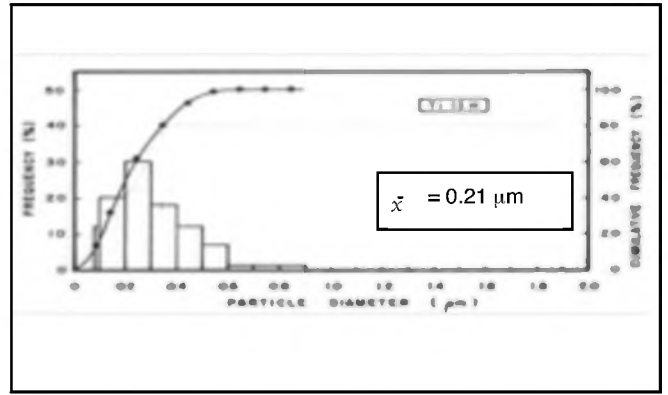


Fig. 9 — Histogram of inclusion sizes observed in the carbon extraction replica of sample Ti 13 H (submerged arc welded sample) (Ref. 23).

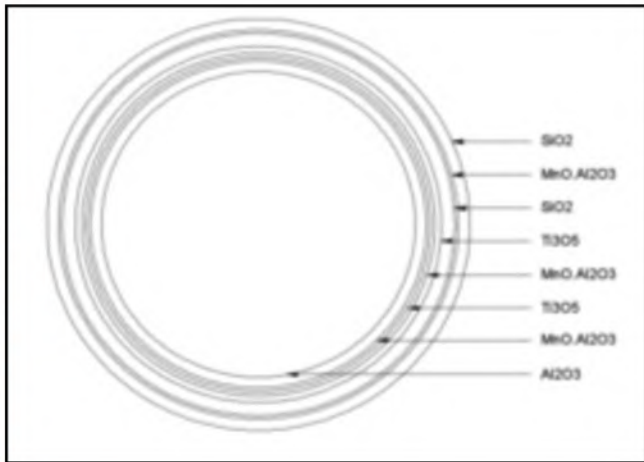


Fig. 10 — Schematic showing complex oxide formation as predicted by the Babu model.

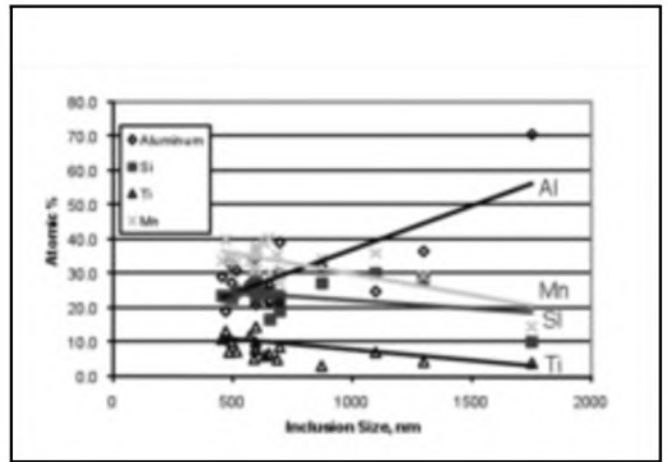


Fig. 11 — Effect of inclusion size on inclusion composition in sample A as measured with EDS.

ever, was significantly lower than in sample Ti 13 H. For example, average acicular ferrite in arc button melts was approximately 40 H_v softer than in sample Ti 13 H. The coarse nature of the button's acicular ferrite could account for the difference in hardness.

Inclusion Analysis

The nucleation of the desirable acicular ferrite microstructure is heavily dependent on the size of the inclusions, diameters greater than 0.2 µm are considered as effective nucleating agents (Ref. 31). A detailed analysis of the nonmetallic inclusions found in the buttons was performed for Sample A.

Special attention must be paid to the characterization of the size distribution of an inclusion population as seen in polished samples. The true diameter of an inclusion is likely to be larger than what is observed

in a micrograph. One possible approach is to dissolve the matrix using a dilute nitric acid solution to gain a perspective on the true diameter, but this technique loses information about the number density, which is also important. Nucleation of acicular ferrite requires a sufficient number of particles for efficient nucleation. Using a selective digestion process, in conjunction with a separate SEM observation of inclusions in a mounted sample is another option, but requires twice as many steps to realize the information.

In this study, a carbon extraction replica was used for comparison purposes. The carbon extraction replica process can yield information about number density and true size distribution using a single process. This process was also chosen by Liu (Ref. 23) to characterize the inclusions present in SAW samples. The carbon extraction replica process is detailed by Ashby et al. (Ref. 32), where the volumet-

ric number density, N_v , is related to the area number density as follows:

$$-\frac{N_v}{N_s} = \frac{1}{x_{Al}} \left\{ 1 + \left(\frac{\sigma_{Al}}{x_{Al}} \right)^2 \right\} \quad (1)$$

where N_s is the number of inclusions per mm², x_{Al} is the average inclusion diameter observed, and σ_{Al} is the standard deviation in mm. In this work, a total of 64 inclusions were observed over nine squares in a standard TEM grid with 100 µm square holes. This translates to an area number density of 911 inclusions per mm² in the sample. The mean inclusion diameter observed was 730 nm, with a standard deviation of 340 nm. This results in a volumetric number density of 1.5×10^{15} inclusions per m³ or 1.5×10^6 inclusions per mm³.

Figures 8 and 9 show histograms of observed diameters for Sample A and sample Ti 13 H. The majority of inclusions in Sample A fell between the range of 250

and 700 nm. Several inclusions larger than 1500 nm were also observed. While most of the inclusions were in the correct range for nucleating acicular ferrite, the mean diameter was larger and volume number density was smaller than the population observed in sample Ti 13 H (210 nm and 1.46×10^8 inclusions/mm³). Kluku and Grong also used carbon extraction replicas to characterize inclusions from SAW samples for composition and size. They measured number densities of 10^8 /mm³ (Refs. 33, 34). These data suggest that the button melt process is producing inclusions with larger size distributions than a real-world welding process. The larger inclusion size could be due to the hold time (25 s) necessary to achieve proper mixing of ingredients.

Comparison with Other Techniques, Discussion, and Recommendations

Additional validation of the button melting technique is proposed here, measurements from the samples made were compared with data available from other techniques including two mathematical models of inclusion number density, an estimated austenitic grain size, and a mathematical model of inclusion composition.

Inclusion Density

It is possible to use an overall transformation kinetics theory model to predict the inclusion nucleation and growth during the welding process. In this study, a numerical model developed by Babu (Ref. 25) based on transformation kinetics was used to gain further insight into the effects of a longer melt time on the inclusion population. For simplicity, the model will be referred to as the Babu model. The button melt process was modeled using the chemistry measured by LECO and ICP as the input composition. In the model, it was necessary to manipulate the heat input and preheat temperature to achieve the hold time and cooling curve of the button melt process. Values of 6 kJ/mm and 1500 K were selected to realize a melt, hold, and solidification time of approximately 25 s in total. For these conditions, the Babu model predicts a number density of 4.47×10^5 inclusions per mm³, and an inclusion diameter of 1.2 μ m. When the welding parameters from sample Ti 13 H (corresponding to 0.8 s melt time) are input into the model, the number density rises to 1.47×10^8 inclusions per mm³, and the diameter shrinks to 0.17 μ m. While predicted average diameter is slightly smaller than observed for sample Ti 13 H, the number density prediction is close to the observed value.

The measured number density for the button (Sample A) (1.5×10^6 inclusions

per mm²) is much lower than observations of others. Kluku and Grong (Refs. 33, 34) measured number densities of 10^8 /mm³ in submerged arc welds. Sample Ti 13 H had 3.3×10^8 inclusions per mm³. It is possible that the carbon extraction process failed to extract a significant fraction of the inclusions. However, observations of mounted samples under electron backscatter mode also revealed a sparse inclusion population. It is more likely that inclusion growth occurred during the melting process. It is also possible to have coalescence of inclusions (Ref. 35). The inclusions appeared to be spherical in nature as observed by SEM. Although it is possible to observe oxides in the interrupted stage of coalescence, no oxides were observed in this state. Another way to study the amount of inclusions is by looking at their volume fraction, which can be determined using the following formula:

$$V_f = N_v \frac{\sum_{i=1}^n \frac{4}{3} \pi r_i^3}{n} \quad (2)$$

Where N_v is volumetric number density calculated in Equation 1, r_i is the measured radius of inclusion i , and n is the total number of inclusions measured. The resulting volume fraction was 5.7×10^{-4} .

Kluku and Grong found that inclusion volume fraction in submerged arc welds will depend on composition according to the following equation:

$$V_f = 10^{-2}[5.0(O) + 5.4(S - 0.003)] \quad (3)$$

where O and S represent the amounts of oxygen and sulfur in wt-% (Ref. 33). The prediction by Grong using Equation 3 gives a value of 5×10^{-4} if the sulfur term is ignored, very close to what was measured. The sulfur term can be ignored because sulfur in this case is lower than the solubility limit in steel, and does not contribute to inclusion formation.

The agreement between measured and predicted values of inclusion volume fraction gives confidence that all inclusions were extracted during the carbon extraction replica process. While the volume fraction is in line with Kluku's and Grong's prediction of what would be expected during welding, the average diameter observed was larger, and the number density was smaller. These findings, along with the comparison of the various hold times using the Babu model, would suggest the button melts experience greater inclusion growth and/or coalescence during the melting process than during a SAW process.

The nucleation and growth of oxides in the melt requires special considerations that should be taken into account in future implementations of this technique. At

melt temperatures above approximately 2000°C, liquid should be the only stable phase according to Thermo-Calc®. If the temperature remains above 2000°C, oxide formation would not occur until the arc is extinguished. The maximum temperature of the molten liquid in the button during the melting process is unknown. Because the arc is a highly localized heat source, it is suspected that temperature fluctuates widely as the electrode is rotated. As the tip-to-work distance is increased, the arc cone becomes larger and less localized. It seems that although the inclusion number density was much lower than a welding process, there were still sufficient nucleation sites for efficient acicular ferrite formation considering the high-volume fraction of acicular ferrite observed in the micrographs. A higher number density would most likely result in a finer microstructure, similar to the microstructure observed in sample Ti 13 H.

Austenite Grain Size

Austenite grain growth will also depend on the inclusion size distribution and number density (Refs. 36–38). While large particles do not pin the grain austenite grain boundary, smaller particles exert a drag force limiting grain growth. The Zener-Smith relationship for austenite grain diameter D_L is

$$D_L = \frac{2d}{3f} \quad (4)$$

where d is the average particle size and f is the volume fraction of inclusions.

It is possible to predict the prior austenite grain size using the measured inclusion parameters with the Zener-Smith relationship developed in Equation 4. Using the calculated volume fraction of 0.00057 and the average inclusion size of 0.7 μ m, the expected prior austenite grain size is 818 μ m. This value is approximately one order of magnitude greater than the 80 μ m measured by Liu for sample Ti 13 H. The reduced fraction of grain boundary ferrite observed in the buttons may be caused not only by the high levels of boron, but also by the enlarged austenite grains.

Inclusion Composition

It is also possible to use computational thermodynamic models to predict the inclusion chemical composition. Table 5 shows predictions from the Babu model for the chemical composition of inclusions forming during the button melt process and during the welding process.

The model does not predict any significant changes in inclusion composition for

the 25-s hold time expected in the button vs. no hold time as expected during welding. Using thermodynamics and kinetic growth equations, the Babu model predicts the order of formation for the inclusions. The first oxide to become stable during cooling is Al_2O_3 , which forms the core of the inclusion. As the weld metal cools and other oxides become stable, layers begin to form sequentially as shown in Fig. 10. It should be noted, however, that the model is phenomenological and not a true representation of the structure. As cooling occurs, multiple oxide phases become thermodynamically stable and will continue to precipitate; thus, clearly delineated layers are not expected. The model is useful in predicting when the various phases begin to form as well as the relative volume fraction of each phase.

According to the Babu model, SiO_2 will be the last oxide to form and would therefore be expected to be present in greater concentrations on the inclusion surface. It may therefore act as the substrate for heterogeneous nucleation of acicular ferrite. It is assumed a spherical inclusion is a simplification that allows the diameter to be calculated and the final layer in this case is expected to be SiO_2 . These findings are significant because most of the literature on acicular ferrite nucleation places emphasis on the importance of titanium on inclusion nucleation of acicular ferrite. The Babu model predicted that roughly 50% of the inclusion would be comprised of aluminum while the measured value averaged about 30% with the difference being made up with increased manganese levels.

Energy-dispersive spectrometry (EDS) was used to characterize the chemical compositions of 21 inclusions found in the extracted replica. Table 6 compares the average composition for the inclusions that were evaluated with those measured in sample Ti 13 H (Ref. 23).

Inclusions in samples A and Ti 13 H contained similar amounts of manganese and silicon. The difference was the amount of aluminum and titanium measured with Sample A containing a larger fraction of both elements. Inclusion composition was observed to be dependent on size as illustrated in Fig. 11.

There is a trend of increasing aluminum with increasing size. Relative amounts of titanium, silicon, and manganese all decrease with increasing size. Manganese decreases most sharply. Aluminum oxides are stable at the highest temperatures and are therefore the first to form during cooling. Inclusions nucleating first have more time to grow. The additional time for growth will occur at a temperature where Al_2O_3 is stable, and would therefore have a higher aluminum composition. Since the button melted samples had a larger average diam-

eter than sample Ti 13 H, the higher aluminum content is expected.

Discussion

The goal of the project was to develop a methodology for expedient welding consumable development by way of a melting process designed to simulate welding conditions. Microstructures for multiple compositions can be evaluated without creating new spools of consumables. This process has some inherent limitations and further steps are required before the consumable can be finalized. In the case of SAW, dilution effects and slag additions would need to be accounted for. Therefore, thermodynamic modeling and button melting experimentation represent the initial work required to develop consumables.

Recommendations

The button melting technique developed was able to mimic the cooling rate, composition, and microstructure of a specific weld created by the SAW process. The technique still needs improvement in several areas including amount of time in molten state and control of oxygen and boron in the melt. It is also desirable to simulate the range of cooling conditions that are expected during various welding processes. Modification and/or further experimentation may be necessary to develop melting processes that simulate these conditions.

The amount of time in the molten state was longer than in the target weld because it was necessary to ensure complete and homogeneous melting of all the solid charge. This resulted in larger inclusions than intended because of the longer time for coarsening. This longer melt time also allowed oxide inclusions to float to the surface and be lost as slag. The lower amount of oxides in the melt could not be compensated for by increasing the oxygen potential in the atmosphere because the large oxides still floated away, while the larger amount of oxide created an oxygen barrier at the surface.

It is recommended that the amount of time in the molten state is reduced to match the time in an actual weld. To achieve homogeneity in this situation, it might be desirable to start with a precompressed charge, so no powders, chips, or small pieces of wire are scattered in the initial melt area. Also, a more powerful torch might be able to create the melt faster.

Conclusions

- The arc button melter technique presented here was able to reproduce the

chemistry and cooling rates of a submerged arc welded sample. Particularly significant is the innovative control of oxygen content in the button melt.

- The button melts reproduced the microstructure of equivalent submerged arc welds; however, with a coarser microstructure and lower hardness.

- Inclusion volume fraction in the arc button melts was similar to the equivalent actual weld, but the inclusions were larger in diameter and lower in number density.

Acknowledgments

The authors wish to thank Tenaris/Confab, Tenaris/Tamsa, NSF CAREER Award DMI-0547649, and the Goierri Foundation for sponsoring this project. Gaizka Sarasola, Miren Lopetegui, and Dianabasi E. Etuk provided invaluable assistance as undergraduate research assistants.

References

1. Alexandrov, B. T., and Lippold, J. C. 2005. A new methodology for studying phase transformations in high strength steel weld metal. *Trends in Welding Research, 7th International Conference*. ASM International, Pine Mountain, Ga.
2. Alexandrov, B. T., and Lippold, J. C. 2006. In-situ weld metal continuous cooling transformation diagrams. *Welding in the World* 50(9-10): 65-74.
3. Anderson, T. D., et al. 2007. The influence of molybdenum on stainless steel weld microstructures. *Welding Journal* 86(9): 281-s to 292-s.
4. Kuwana, T., and Sato, Y. 1983. Absorption of oxygen into iron weld metal during arc welding. Report 2: Absorption into iron weld metal in Ar- CO_2 gas mixture. *Quarterly Journal of the Japan Welding Society* 1(1): 16-21.
5. Kuwana, T., and Sato, Y. 1986. Absorption of oxygen into iron weld metal during arc welding. *Transactions of the Japan Welding Society* 17(2): 124-132.
6. Kuwana, T., and Sato, Y. 1987. Oxygen absorption and oxide inclusion of iron weld metal during arc welding. *Quarterly Journal of the Japan Welding Society* 5(3): 396-402.
7. Kuwana, T., and Sato, Y. 1988. Oxygen absorption and oxide inclusion of iron weld metal during arc welding. *Transactions of the Japan Welding Society* 19(2): 134-142.
8. Kuwana, T., and Sato, Y. 1989. Effect of additional elements on oxygen absorption by steel weld metal during arc welding. Part 3: Oxygen absorption by Fe-Al weld metal. *Quarterly Journal of the Japan Welding Society* 7(3): 330-335.
9. Kuwana, T., and Sato, Y. 1989. Effect of silicon on oxygen absorption by steel weld metal during arc welding. *Transactions of the Japan Welding Society* 20(1): 37-44.
10. Kuwana, T., and Sato, Y. 1989. Effect of additional elements on oxygen absorption by steel weld metal during arc welding. Part 1: Oxygen absorption by Fe-Si weld metal. *Quarterly Journal of the Japan Welding Society* 7(1): 43-49.
11. Kuwana, T., and Sato, Y. 1989. Effect of

additional elements on oxygen absorption by steel weld metal during arc welding. Part 2: Oxygen absorption by Fe-Mn and Fe-Si-Mn weld metal. *Quarterly Journal of the Japan Welding Society* 7(1): 49–56.

12. Kuwana, T., Sato, Y., and Kaneda, S. 1992. Oxygen absorption and oxide inclusion of Fe-Cr weld metal. *Quarterly Journal of the Japan Welding Society* 10(3): 397–402.

13. Kuwana, T., Sato, Y., and Kaneda, S. 1993. Oxygen absorption and oxide inclusions in Fe-Cr weld metal. *Welding International* 7(5): 365–370.

14. Kuwana, T., Sato, Y., and Onodera, N. 1991. Oxygen absorption and deoxidation of steel weld metal. Part 1: Oxygen absorption of arc melted pure iron. *Quarterly Journal of the Japan Welding Society* 9(3): 405–409.

15. Kuwana, T., Sato, Y., and Onodera, N. 1991. Oxygen absorption and deoxidation of steel weld metal. Part 2: Oxygen absorption and deoxidation of arc melted Fe-Si alloy. *Quarterly Journal of the Japan Welding Society* 9(3): 410–415.

16. Kuwana, T., et al. 1991. Oxygen absorption and oxide inclusions in Fe-Ti weld metal. *Welding International* 5(2): 89–94.

17. Sato, Y., and Kuwana, T. 1995. Oxygen absorption in iron and steel weld metal. *ISIJ International* 35(10): 1162–1169.

18. Sato, Y., Kuwana, T., and Takeda, S. 1996. Oxygen absorption by pure iron weld metal in gas tungsten arc (TIG) welding. *Welding International* 10(6): 461–465.

19. Sato, Y., Kuwana, T., and Tomita, N. 1993. Oxygen absorption of steel weld metal during gas metal arc welding. *Welding International* 7(4): 280–285.

20. Sato, Y., Tomita, K., and Kuwana, T. 1992. Oxygen absorption by steel weld metal during GMA welding. Part 1: Oxygen absorption by steel weld metal in Ar-O₂, Ar-CO₂, and CO₂-O₂ welding atmosphere. *Quarterly Journal of the Japan Welding Society* 10(3): 384–390.

21. Sato, Y., Tomita, K., and Kuwana, T. 1992. Oxygen absorption by steel weld metal during GMA welding. Part 2: Oxygen absorption by steel weld metal in Ar-CO₂-O₂ welding atmosphere. *Quarterly Journal of the Japan Welding Society* 10(3): 390–396.

22. Sato, Y., Tomita, K., and Kuwana, T. 1993. Oxygen absorption by steel weld metal in an Ar-CO₂-O₂ welding atmosphere. Report 2: Oxygen absorption during gas metal arc welding. *Welding International* 7(5): 358–364.

23. Liu, S. 1986. The role of nonmetallic inclusions in controlling weld metal microstructures in niobium microalloyed steels, in metallurgical and materials engineering. PhD dissertation, Colorado School of Mines, Golden, Colo.

24. Liu, S., and Olson, D. L. 1986. The role of inclusions in controlling HSLA steel weld microstructures. *Welding Journal* 65(6): 139-s to 149-s.

25. Babu, S. S., et al. 1999. Model for inclusion formation in low alloy steel welds. *Science and Technology of Welding and Joining* 4(5): 276–284.

26. Granjon, H. 1967. Notes on the carbon equivalent. IIW Document IX.

27. Tordonato, D. S. 2008. A novel approach to the design of welding consumables using computational and physical models. PhD dissertation. Colorado School of Mines, Golden, Co.

28. Gibbs, J. 1987. Analysis by inductively

coupled plasma-emission spectrometry. *Metals and Materials*. February.

29. *Compendium of Weld Metal Microstructures and Properties*. 1985. The Welding Institute, Cambridge, UK.

30. Snieder, G., and Kerr, H. W. 1984. Effects of chromium additions and flux type and structure and properties of HSLA steel submerged arc weld metal. *Canadian Metallurgical Quarterly* 23(3): 315–325.

31. Abson, D. J. 1989. Non-metallic inclusions in ferritic steel weld metals — A review. *Welding in the World* 27(3/4): 11–28.

32. Ashby, M. F., and Ebeling, R. 1966. On the determination of the number, size, spacing, and volume fraction of spherical second-phase particles from extraction replicas. *Transactions of the Metallurgical Society of AIME* 236(10): 1396–1404.

33. Klukun, A. O., and Grong, O. 1989. Mechanisms of Inclusion Formation in Al-Ti-Si-Mn Deoxidized Steel Weld Metals. *Materials Science and Engineering A — Structural Materials, Properties, Microstructure, and Processing* 20A(8): 1335–1349.

34. Klukun, A. O., Grong, O., and Hjelen, J. 1988. SEM based automatic image analysis of nonmetallic inclusions in steel weld metals. *Materials Science and Technology* 4(7): 649–654.

35. Babu, S. S., David, S. A., and Deb Roy, T. 1996. Coarsening of oxide inclusions in low alloy steel welds. *Science and Technology of Welding and Joining* 1: 17–27.

36. Ramsay, C. W. 1989. The influence of oxygen and non-metallic inclusions on high strength steel weld metal microstructures and properties, PhD dissertation. Colorado School of Mines, Golden, Co.

37. Smith, C. S., 1948. Grain, phase, and interfaces: An interpretation of microstructures. *Trans. AIME*, 175.

38. Fleck, N. A., 1984. The effect of filler wire and flux compositions on the microstructure of

microalloyed steel weld metal, PhD dissertation. Colorado School of Mines, Golden, Co.

Appendix

Procedure for Button Melting Process

- Clean and sharpen electrode to an angle of 22 deg.
- Clean crucible with ethanol and steel wool.
- Charge crucible and load into chamber. Powders should be placed near the bottom of the charge to avoid displacement during arc initiation.
- Set electrode protrusion at 0.75 in. (19 mm).
- Set gas flow typical values: 17.5 ft³/h (argon), 145 c³/min (oxygen).
- Set welding parameters: 150 A.
- Open coolant.
- Wait two minutes.
- Start the arc.
- Position the copper sheath so that the arc diameter is approximately the same size as the charge.
- Rotate torch counterclockwise around the sample until the sample is completely molten. Melt for 25 s (approximately 30 rotations).
- Terminate the arc.
- Allow sample to cool at least 200 s prior to removal of the copper crucible.
- Turn the sample over, push any loose granules to the center of crucible.
- Remelt using the same technique for 20 s (20 rotations).

Underwater Welding Workshop

The 3rd International Workshop on the “State of the Art, Science and Reliability of Underwater Welding and Inspection Technology” will be held at the Sheraton Suites (Galleria) in Houston, Texas, November 17-19, 2010. The Workshop will examine recent developments in underwater welding and inspection and define the state of engineering and the practice of underwater welding and inspection of fixed and floating marine structures and pipelines. The event will be co-sponsored by the Bureau of Ocean Energy Management, Regulation, and Enforcement (BOEMRE), Pipeline & Hazardous Materials Safety Administration (DOT-PHMSA), American Bureau of Shipping, American Welding Society, and American Society of Nondestructive Testing. For more detailed information regarding programming, registration, participation, and sponsorship, please access: <http://csmospace.com/uwit/>